



# High Q-factor, ultrasensitivity slot microring resonator sensor based on chalcogenide glasses

XUELEI ZHANG,<sup>1,2</sup> CHENFENG ZHOU,<sup>1,2</sup> YE LUO,<sup>3,4</sup> ZHEN YANG,<sup>1,2</sup>  
WEI ZHANG,<sup>1,2,6</sup>  LAN LI,<sup>3,4</sup>  PEIPENG XU,<sup>1,2,7</sup>  PEIQING  
ZHANG,<sup>2</sup> AND TIEFENG XU<sup>5</sup>

<sup>1</sup>Faculty of Electrical Engineering and Computer Science, Ningbo University, Ningbo 315211, China

<sup>2</sup>Key Laboratory of Photoelectric Detecting Materials and Devices of Zhejiang Province, Ningbo 315211, China

<sup>3</sup>Key Laboratory of 3D Micro/Nano Fabrication and Characterization of Zhejiang Province, School of Engineering, Westlake University, 18 Shilongshan Road, Hangzhou 310024, China

<sup>4</sup>Institute of Advanced Technology, Westlake Institute for Advanced Study, 18 Shilongshan Road, Hangzhou 310024, China

<sup>5</sup>Ningbo Institute of Oceanography, Ningbo University, Ningbo 315211, China

<sup>6</sup>zhangwei3@nbu.edu.cn

<sup>7</sup>xupeipeng@nbu.edu.cn

**Abstract:** In this article, the chalcogenide slot waveguide is theoretically studied, and the highest power confinement factors of the slot region and the cladding region are obtained to be 36.3% and 56.7%, respectively. A high-sensitivity chalcogenide slot microring resonator sensor is designed and fabricated by electron-beam lithography and dry etching. The structure increases the sensitivity of the sensor compared with the conventional evanescent field waveguide sensor. The cavity has achieved a quality factor of  $1 \times 10^4$  by fitting the resonant peaks with the Lorentzian profile, one of the highest quality factors reported for chalcogenide slot microring resonators. The sensor sensitivity is measured to be 471 nm/RIU, which leads to an intrinsic limit of detection of  $3.3 \times 10^{-4}$  RIU.

© 2022 Optica Publishing Group under the terms of the [Optica Open Access Publishing Agreement](#)

## 1. Introduction

Chalcogenide glasses (ChGs), which contain one or more group VI elements of S, Se, and Te with other low-electronegativity elements, such as As, Sb, Ge, or Ga [1–3], have been proven to be high-performance optical materials for integrated photonic applications. The optical characteristics of ChGs are reflected in the wide transparency window extending from the visible to the far-infrared, high linear refractive indices, high Kerr nonlinearity, low two-photon absorption, and flexible structures [4–7]. Based on these merits, ChGs have been extensively applied in optical storages [8], optical amplifiers [9], optical sensors [10], and lasers [11].

Over the past few decades, optical sensor devices based on different materials, such as group IV materials, metal materials, and semiconductor materials, have been reported [12–15]. Versatile structures, including microring resonators [16], photonic crystals [17], Mach-Zehnder interferometers [18], and Bragg gratings [19], have been proposed and investigated. On-chip microring resonators, a type of representative photonic structure providing high sensitivity, compact size, and label-free properties, have been extended to different sensing areas, such as biosensors [20,21], chemical sensors [22], temperature and humidity sensors [23,24], and pressure sensors [25]. Furthermore, the on-chip microring resonator is compatible with complementary metal-oxide-semiconductor, and it could be easily manufactured [26–28]. However, conventional strip waveguide microring resonators confine the effective mode in the higher index waveguide

core layer, and only weak evanescent field interacts with the outside lower index cladding, thus limiting the sensitivity of devices. Slot waveguide microring resonators, which confine the effective mode in the low index slot region [29], could increase the interaction between the effective mode and the analyte. To date, slot microring resonators have been widely investigated in silicon-based platforms [30–32], but slot microring resonators based on ChGs have been rarely reported [33].

In this work, a ChG slot (ChGS) microring resonator is presented, and  $\text{Ge}_{28}\text{Sb}_{12}\text{Se}_{60}$  (GeSbSe) film ( $n = 2.72@1550 \text{ nm}$ ) is used as the core layer of the slot microring resonator. The structure parameters of the ChGS microring resonators are investigated, the power confinement factor (PCF) is optimized, and the bend slot waveguide is optimized to improve the sensitivity. 30 kV electron beam lithography (EBL) followed by a dry etching process is applied to fabricate ChGS microring resonators. A high-quality factor (Q-factor) resonator is obtained, based on which a refractive index (RI) sensor is proposed and demonstrated. And the sensitivity and limit of detection (LOD) are also analyzed by different concentrations of NaCl solutions.

## 2. Design and optimization of ChGS waveguide

### 2.1. PCF of ChGS waveguide

The ChGS waveguide was prepared on a silicon substrate with a 2  $\mu\text{m}$ -thick buried  $\text{SiO}_2$  layer. The proposed ChGS waveguide schematic is shown in Fig. 1(a), where the red line indicates the slot region, and the green line indicates the cladding region (including the slot region). The ChGS waveguide has a slot width of  $W_{\text{slot}} = 50 \text{ nm}$ , rail width of  $W_{\text{rail}} = 340 \text{ nm}$ , and height of  $H_{\text{rail}} = 300 \text{ nm}$ . PCF is an important parameter described by the optical field confinement, which quantitatively indicates that the guided modal field is confined in a specific region. The PCF of the slot region ( $\Gamma_S$ ) and cladding region ( $\Gamma_C$ ) could be calculated in Mode Solution using the following equations:

$$\Gamma_S = \frac{\iint_S |E(x, y)|^2 dx dy}{\iint_{\infty} |E(x, y)|^2 dx dy} \quad (1)$$

$$\Gamma_C = \frac{\iint_C |E(x, y)|^2 dx dy}{\iint_{\infty} |E(x, y)|^2 dx dy} \quad (2)$$

where  $E(x, y)$  is the electric field vector, and  $C$  and  $S$  indicate the cladding and slot regions, respectively [34]. According to the simulation results,  $W_{\text{rail}}$  has its greatest impact on PCF.

$W_{\text{rail}}$  were varied to validate the robustness of the designed structure by calculating PCF changes. When  $W_{\text{rail}}$  was set from 270 nm to 450 nm, homologous variation tendency of PCF in the slot region and the cladding region was obtained, as shown in Fig. 1(b). The best PCF was exhibited when  $W_{\text{rail}}$  was 340 nm. As  $W_{\text{rail}}$  continued to increase, the PCF decreased. The maximum values of PCF were  $\Gamma_C = 55.9\%$  and  $\Gamma_S = 36.3\%$ .

### 2.2. Parameters and single-mode condition of ChGS waveguide

The amplitude profile of the E-field is shown in the 3D surface plot shown in Fig. 2(a). The RIs for the GeSbSe core layer ( $n_{\text{rail}}$ ) and  $\text{SiO}_2$  buried layer ( $n_{\text{SiO}_2}$ ) were 2.72 and 1.44, separately. Both sides of the high-index GeSbSe rails confined the light in the low-index air region, thus enhancing the interaction between the light and the analyte to be detected, which leads to increased sensitivity.

The effective RI ( $n_{\text{eff}}$ ) changes were determined when  $W_{\text{rail}}$  varied from 300 nm to 800 nm. The  $n_{\text{eff}}$  and single-mode conditions at the wavelength of 1550 nm are shown in Fig. 2(b). The

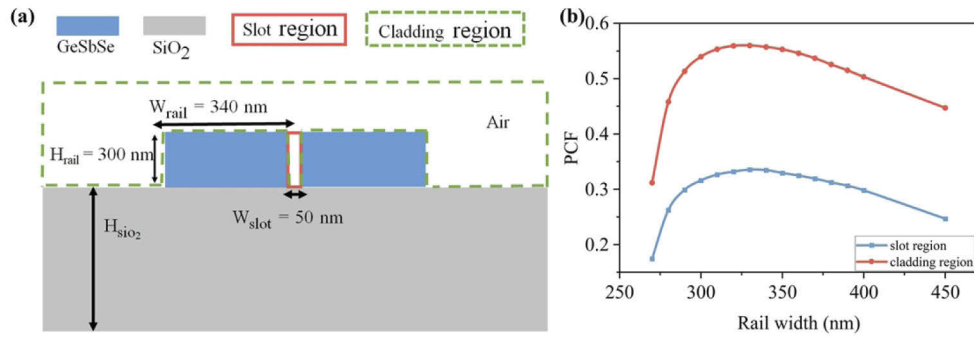


**Fig. 1.** (a) Cross-section views of the designed ChGS waveguide. (b) PCF of the slot region and cladding region as a function of  $W_{\text{rail}}$ .

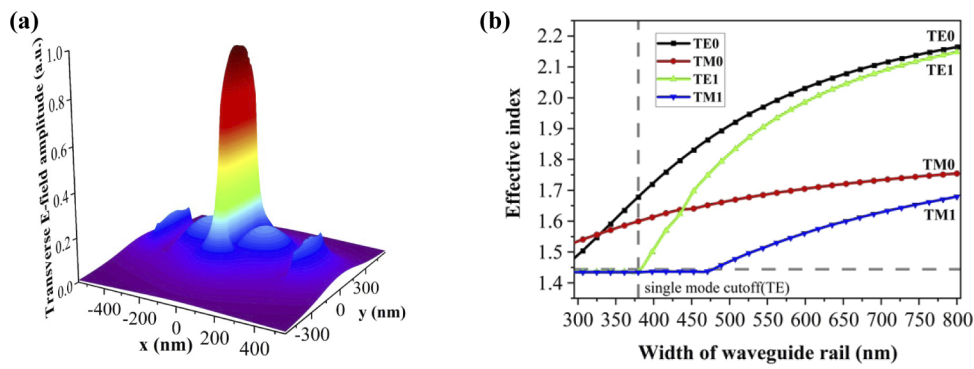


**Fig. 2.** (a) 3D surface plot of the E-field amplitude. (b) Simulation results of the effective index as a function of  $W_{\text{rail}}$ . The slot waveguide is covered with air. Only the modes above the horizontal dashed lines are guided.

modes with effective index greater than  $n_{\text{SiO}_2}$  above the horizontal dashed line were guided. The vertical dashed line indicates the single mode cutoff width, which is the minimum width in which a slot waveguide will only allow TE0 and TM0 to propagate. If  $W_{\text{rail}}$  is over this width, higher order modes, i.e., TE1, TM1, etc. will be able to propagate.

### 3. Design and fabrication of ChGS microring resonators

#### 3.1. Design of ChGS microring resonators

Figure 3(a) shows the designed structure of the ChGS microring resonator. The resonator contains a GeSbSe strip bus waveguide acting as input and output ports and a GeSbSe slot microring acting as the resonator, in which  $W_{\text{out,rail}}$  is the width of the outer ring, and  $W_{\text{in,rail}}$  is the width of the inner ring. Figures 3(b) and 3(c) show the electric field distribution with different rail parameters. In Fig. 3(b),  $W_{\text{out,rail}}$  and  $W_{\text{in,rail}}$  were set as  $0.3 \mu\text{m}$ . In Fig. 3(c),  $W_{\text{out,rail}}$  and  $W_{\text{in,rail}}$  were set as  $0.3$  and  $0.34 \mu\text{m}$ , respectively. Figure 3(b) shows that the electric field was biased towards the outer ring when  $W_{\text{out,rail}}$  and  $W_{\text{in,rail}}$  had the same value, in accordance with the bending effect [35,36]. This phenomenon could decrease the interaction between the light and the analyte in the slot region and reduce the sensitivity. Reducing  $W_{\text{out,rail}}$  to avoid the bending effect and improve the coupling efficiency is a double benefit that could address this problem. Thus, the following parameters were determined for the structure of ChGS microring

resonators: the inner ring radius ( $R_{in}$ ) is  $60\ \mu\text{m}$ , the width of the strip bus waveguide ( $W_{strip}$ ) is  $0.6\ \mu\text{m}$ ,  $W_{out,rail}$  is  $0.3\ \mu\text{m}$ , and  $W_{in,rail}$  is  $0.34\ \mu\text{m}$ .

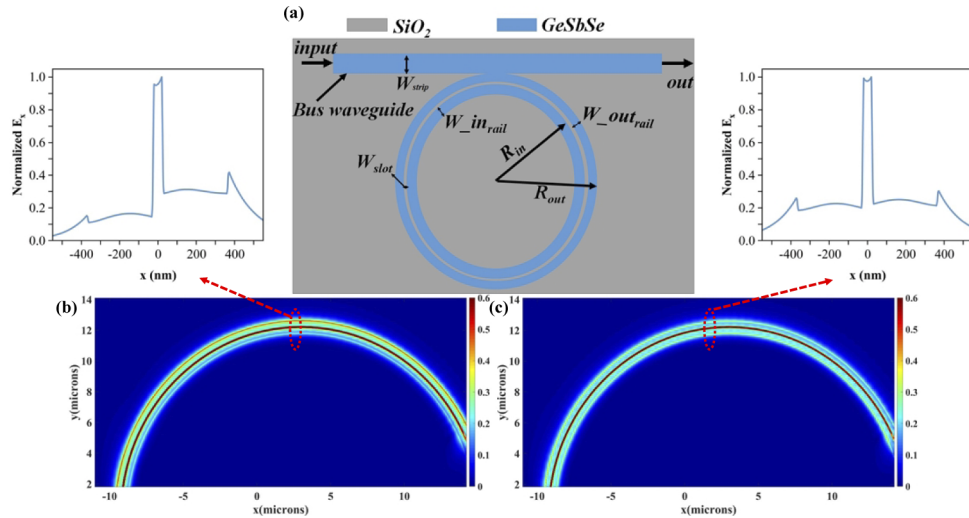


**Fig. 3.** (a) Schematic of proposed ChGS microring resonator. (b) Electric field distribution with  $W_{out,rail} = 0.3\ \mu\text{m}$  and  $W_{in,rail} = 0.3\ \mu\text{m}$ . (c) Electric field distribution with  $W_{out,rail} = 0.3\ \mu\text{m}$  and  $W_{in,rail} = 0.34\ \mu\text{m}$ . Inserts are normalized transverse electric field distribution of the cross section.

### 3.2. Fabrication of ChGS microring resonators

A  $300\ \text{nm}$ -thick GeSbSe thin film was prepared by thermal evaporation on  $\text{SiO}_2$  cladding. Figure 4(a) shows the real and imaginary parts of the RI of the GeSbSe layer. The roughness of the GeSbSe film was determined as  $0.373\ \text{nm}$  of RMS by atomic force microscopy (in Fig. 4(b)), which showed high-quality GeSbSe film.

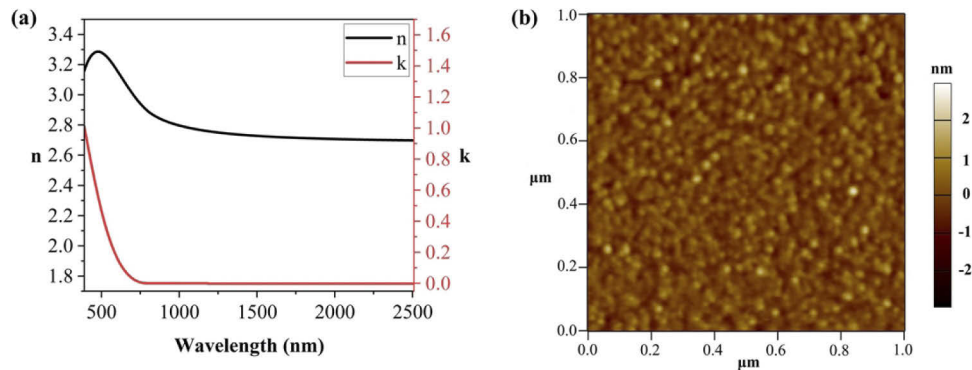


**Fig. 4.** (a) RI of GeSbSe film at a wavelength of  $0.4\text{--}2.5\ \mu\text{m}$ . (b) AFM image of  $300\ \text{nm}$  GeSbSe film.

The EBL technique (Raith eLINE Plus) was applied to transfer the designed ChGS microring resonators and grating couplers patterns onto a photoresist (ARP 6200) layer. A ChGS waveguide was fabricated first to determine the optimal etching parameters and process. After the development of the resist, the sample was baked on a hotplate for 1 min at  $130^\circ\text{C}$  before the etching

process. Four different chemical gases, namely, trifluoro-methane ( $\text{CHF}_3$ ), carbon-tetrafluoride ( $\text{CF}_4$ ), oxygen ( $\text{O}_2$ ), and argon ( $\text{Ar}$ ), were used to etch the ChGS microring resonators and grating couplers by using an inductively coupled plasma etcher (Oxford 100). First, the chip was preprocessed by a gas mixture of  $\text{O}_2$ - $\text{CHF}_3$ - $\text{Ar}$  in a 30:3:2 flow ratio. Then, the gas mixture of  $\text{CHF}_3$ - $\text{CF}_4$  in a 2:1 flow ratio was induced to etch the GeSbSe layer, with a power of 300 W. The top-view SEM image of the ChGS waveguide is shown in Fig. 5(a), which demonstrates a satisfactory etching result with vertical sidewalls.

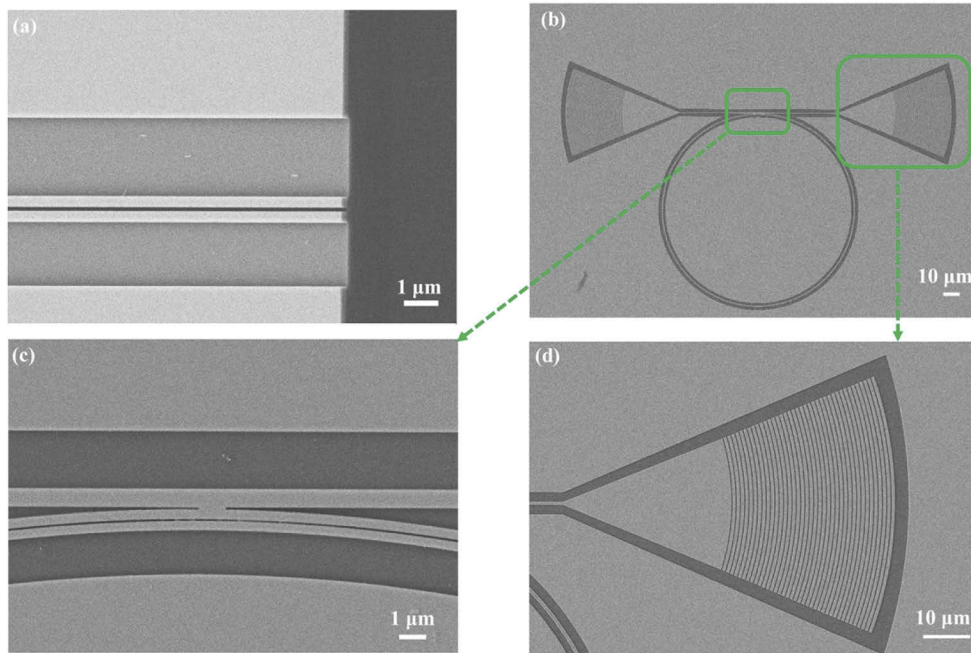


**FIG. 5.** (a) Top view of the fabricated ChGS. (b) SEM micrograph of the fabricated ChGS microring resonator device. (c) Coupling region between the bus waveguide and the microring resonator. (d) SEM image of the focusing grating coupler.

Then, ChGS microring resonators were obtained using the same optimized anisotropic etching process, as shown in Fig. 5(b). The enlargements of the coupling region and the grating coupler are shown in Figs. 5(c) and 5(d), respectively. The full-etched grating coupler for TE polarization, located at both ends of the ChGS microring resonator, has a period of  $0.962 \mu\text{m}$  and a duty cycle of 0.74. It is notable that the fabrication error between the designed and fabricated structure parameters is about  $\pm 25 \text{ nm}$ .

### 3.3. Measurement and sensing experiment

The transmission spectra of ChGS microring resonator device were measured by the built-up system shown in Fig. 6(a). The system contained a tunable laser (Santec TSL-550) ranging from 1500 nm to 1610 nm, and a polarization controller (Thorlabs FPC526) was used to ensure the TE mode light was coupled into the ChGS microring resonator through the single-mode fiber (SMF) with an incident angle of  $10^\circ$ . Another SMF was connected to the power meter (Santec MPM210) to collect the output light from the bus waveguide and obtain the transmission spectrum.

Then, an RI sensing experiment of NaCl solutions was performed. Theoretically, changes in the  $n_{\text{eff}}$  of the device give rise to the variation of resonator wavelength. In this experiment, NaCl solutions with concentration changes from 0% to 2% were dropped onto the surface of the

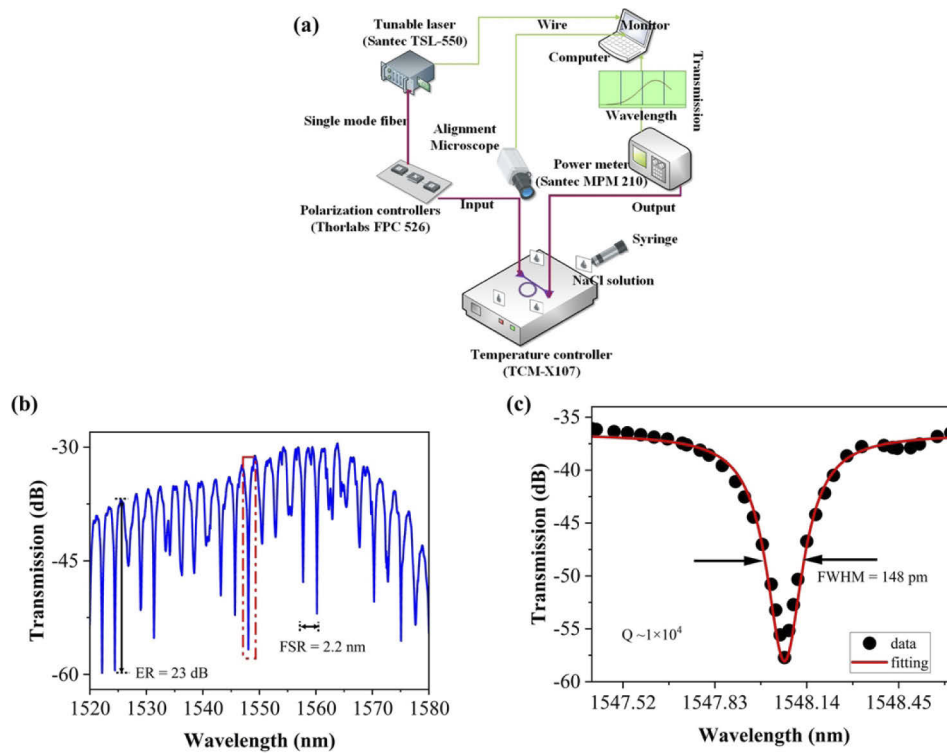


**Fig. 6.** (a) Schematic of the characterization setup. (b) Transmission spectrum of the ChGS microring resonator with  $R_{in} = 60 \mu\text{m}$ . (c) Single resonance peak with a Lorentzian fit to extra Q-factor. Experimental transmission (black points) and Lorentzian fitting (red line) of these transmission spectra.

ChGS microring resonator device. Changes in  $n_{eff}$  could be probed, and wavelength variations were manifested. During the experiment, a thermoelectric cooler was placed on the bottom to maintain the temperature at  $20^\circ\text{C}$  to eliminate thermal drift.

## 4. Results and discussions

### 4.1. Performance of ChGS microring resonators

The output transmission spectrum with the wavelength of 1520-1580 nm with the tuning step of 0.005 nm is illustrated in Fig. 6(b). The critical coupling resonance is quantified by an extinction ratio higher than 20 dB [37], and the experimental extinction ratio was measured up to 23 dB, and the free spectral range was  $\sim 2.2$  nm. The ratio of the resonance wavelength ( $\lambda_{res}$ ) to the peak of resonance full-width-at-half-maximum ( $\Delta\lambda_{FWHM}$ ) is defined as Q-factor:

$$Q = \frac{\lambda_{res}}{\Delta\lambda_{FWHM}} \quad (3)$$

Figure 6(c) shows one resonant peak outlined in red in Fig. 6(b), as fitted via Lorentzian fit. The resonance wavelength was 1548.06 nm, and the  $\Delta\lambda_{FWHM}$  was 148 pm, while a Q-factor of  $\sim 1 \times 10^4$  was achieved.

A notable detail is that the Q-factor was lower than that of strip microring and microdisk with similar ChGs material [38–40], mainly because ChGS microring resonators possess mode mismatch, higher bending loss, and scattering loss than conventional microring resonators.

Utilizing atomic layer deposition of dielectric films, such as TiO<sub>2</sub> [41,42], is a method to reduce propagation losses. However, it brings in redundant procedures and increases the cost. Another method may be to improve the coupling efficiency [43]. However, the structure of the ChGS microring resonator benefits the application of RI sensing, as discussed below.

#### 4.2. Sensitivity and LOD of RI sensors

Figure 7(a) shows the transmission spectrum shifting during the NaCl solution sensing experiment. The slot region and upper cladding region were filled with NaCl solutions under different concentrations in the experiment. As the concentrations of the NaCl solution increased, the resonance wavelength also increased. The NaCl solution concentration ranged from 0% to 2% with a 0.5% step, and the homologous RI ranged from 1.333 to 1.337, contributing to the change in the upper cladding. The RI increased by 0.0018 RIU for NaCl concentration, increasing 1% at 20°C [44]. Figure 7(b) plots the resonance wavelength shift as a function of NaCl concentration. The RI sensitivity of the sensor is defined as follows:

$$S = \frac{\Delta\lambda_{res}}{\Delta n_{cladding}} \quad (4)$$

where  $\Delta\lambda_{res}$  is the resonance wavelength shift, and  $\Delta n_{cladding}$  is the RI variation in cladding medium. The sensitivity was reflected by the slope of the linear fitting line, and it was calculated to be 471 nm/RIU. The sensitivity was four times higher than the recent reports on high-sensitivity microring resonators [45].

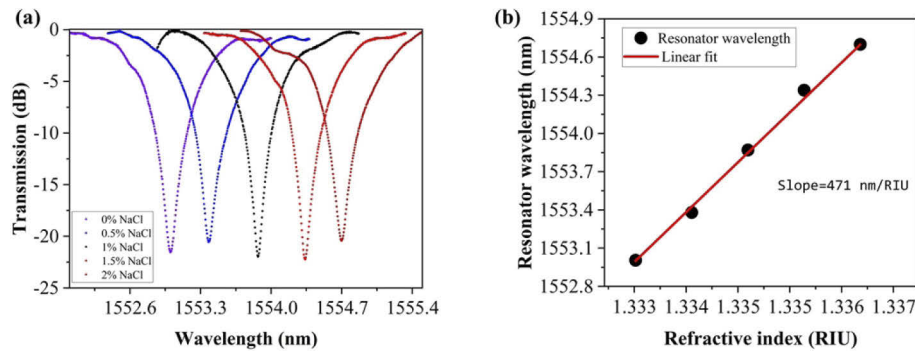


**Fig. 7.** (a) Spectrum shifts along with upper cladding medium (NaCl concentration). (b) Peak wavelength shift as a function of the change in the RI of the NaCl solutions.

LOD could be defined as the minimum detectable RI change. The definition that the change in RI corresponds to one resonator linewidth is characterized as the intrinsic device performance. This definition is also known as intrinsic LOD as follows [46]:

$$iLOD = \frac{\lambda_{res}}{QS} \quad (5)$$

where  $\lambda_{res}$  is the resonance wavelength, and Q and S are the quality factor and sensitivity of the device. The experimental results above obtained an intrinsic LOD of  $\sim 3.3 \times 10^{-4}$  RIU.

Table 1 summarizes the features of some slot microring resonators on silicon-based materials and ChGs in near infrared. It is notable that our work with ChGs is slightly less sensitive than that in [22] and [30], but with a larger Q-factor. Compared with other devices listed in the table, our work shows advantages both in Q-factor and sensitivity, although with a relatively large radius, which indicates the feasibility of high Q-factor, ultrasensitivity and reasonable LOD slot microring resonator sensor for ChGs.

**Table 1. Comparison between reported slot microring resonators based on different materials**

Material	Wavelength (nm)	Radius ( $\mu\text{m}$ )	Q-factor	Sensitivity (nm/RIU)	Reference
Si	1550	10	5000	490	[22]
Si	1550	30	1900	476	[30]
Si	1310	13	330	298	[47]
Si <sub>3</sub> N <sub>4</sub>	1550	50	8610	384	[31]
Si <sub>3</sub> N <sub>4</sub>	1310	70	3000	240	[32]
Si <sub>3</sub> N <sub>4</sub>	1310	50	1800	212	[48]
GeSbSe	1550	60	10000	471	(This work)

## 5. Conclusion

To sum up, a slot waveguide is designed and optimized theoretically based on a high-performance optical material, ChGs. The finite element method based on the mode solver is used for numerical analysis and simulations of the ChGs slot waveguide. PCF is enhanced in the slot region and cladding region to the benefit of designing a ChGS microring resonator and high-sensitivity sensors. The maximum values of PCF are obtained to be  $\Gamma_C = 56.7\%$  and  $\Gamma_S = 36.3\%$ . The ChGS microring resonator could improve the sensitivity compared with traditional strip microring resonator devices. The Q-factor of the ChGS microring resonator is  $\sim 1 \times 10^4$ . RI sensing experiment is carried out to demonstrate the sensitivity. A sensitivity of  $\sim 471$  nm/RIU and an iLOD of  $\sim 3.3 \times 10^{-4}$  RIU in the ChGS microring resonator are measured with  $R_{in} = 60 \mu\text{m}$ . This work shows that ChGS has promising application aspects in mid-infrared field of high-sensitivity sensing.

**Funding.** Natural Science Foundation of Zhejiang Province (No. LD22F040002, No. LD19F050001); National Natural Science Foundation of China (No. 61875099, No. 62175202, No. 12104375); Natural Science Foundation of Ningbo (No. 202003N4007); K. C. Wong Magna Fund in Ningbo University.

**Disclosures.** The authors declare no conflicts of interest.

**Data availability.** Data underlying the results presented in this paper are not publicly available at this time but may be obtained from the authors upon reasonable request.

## References

1. B. J. Eggleton, B. Luther-Davies, and K. Richardson, "Chalcogenide photonics," *Nat. Photonics* **5**(3), 141–148 (2011).
2. C. Lin, C. Rüssel, and S. Dai, "Chalcogenide glass-ceramics: Functional design and crystallization mechanism," *Prog. Mater. Sci.* **93**, 1–44 (2018).
3. A. B. Seddon, "Chalcogenide glasses: a review of their preparation, properties and applications," *J. Non-Cryst. Solids* **184**, 44–50 (1995).
4. J. M. Harbold, F. Ö. Ilday, F. W. Wise, J. S. Sanghera, V. Q. Nguyen, L. B. Shaw, and I. D. Aggarwal, "Highly nonlinear As–S–Se glasses for all-optical switching," *Opt. Lett.* **27**(2), 119–121 (2002).
5. V. G. Ta'eed, N. J. Baker, L. Fu, K. Finsterbusch, M. R. E. Lamont, D. J. Moss, H. C. Nguyen, B. J. Eggleton, D. Y. Choi, S. Madden, and B. Luther-Davies, "Ultrafast all-optical chalcogenide glass photonic circuits," *Opt. Express* **15**(15), 9205–9221 (2007).
6. C. Vignoux-Bercovici, V. Ranieri, L. Labadie, J. E. Broquin, P. Kern, and A. Pradel, "Waveguides based on Te<sub>2</sub>As<sub>3</sub>Se<sub>5</sub> thick films for spatial interferometry," *J. Non-Cryst. Solids* **352**(23-25), 2416–2419 (2006).
7. L. Zhang, W. Zhang, X. Wang, P. Zhang, S. Dai, and Q. Nie, "Investigation of Ge<sub>20</sub>Sb<sub>15</sub>Se<sub>65</sub> photonic crystal slab waveguides with slow light at infrared wavelength," *Opt. Mater. Express* **3**(9), 1438–1443 (2013).
8. Z. Sun, J. Zhou, and R. Ahuja, "Structure of Phase Change Materials for Data Storage," *Phys. Rev. Lett.* **96**(5), 055507 (2006).
9. W. J. Chung, H. S. Seo, B. J. Park, J. T. Ahn, and Y. G. Choi, "Selenide Glass Optical Fiber Doped with Pr<sup>3+</sup> for U-Band Optical Amplifier," *ETRI J* **27**(4), 411–417 (2005).
10. J. Hu, V. Tarasov, A. Agarwal, L. Kimerling, N. Carlie, L. Petit, and K. Richardson, "Fabrication and testing of planar chalcogenide waveguide integrated microfluidic sensor," *Opt. Express* **15**(5), 2307–2314 (2007).

11. A. K. Mairaj, C. Riziotis, A. M. Chardon, P. G. R. Smith, D. P. Shepherd, and D. W. Hewak, "Development of channel waveguide lasers in Nd<sup>3+</sup>-doped chalcogenide (Ga:La:S) glass through photoinduced material modification," *Appl. Phys. Lett.* **81**(20), 3708–3710 (2002).
12. D.-H. Baek and J. Kim, "MoS<sub>2</sub> gas sensor functionalized by Pd for the detection of hydrogen," *Sens. Actuators, B* **250**, 686–691 (2017).
13. C. Blin, Z. Han, H. A. Girard, P. Bergonzo, P. Boucaud, M. El Kurdi, S. Saada, S. Sauvage, and X. Checoury, "Surface-sensitive diamond photonic crystals for high-performance gas detection," *Opt. Lett.* **41**(18), 4360–4363 (2016).
14. Y. Huang, S. K. Kalyoncu, Q. Zhao, R. Torun, and O. Boyraz, "Silicon-on-sapphire waveguides design for mid-IR evanescent field absorption gas sensors," *Opt. Commun.* **313**, 186–194 (2014).
15. M. G. Manera, A. Colombelli, A. Taurino, A. G. Martin, and R. Rella, "Magneto-Optical properties of noble-metal nanostructures: functional nanomaterials for bio sensing," *Sci. Rep.* **8**(1), 12640 (2018).
16. M. Sumetsky, R. S. Windeler, Y. Dulashko, and X. Fan, "Optical liquid ring resonator sensor," *Opt. Express* **15**(22), 14376–14381 (2007).
17. C. Fenzl, T. Hirsch, and O. S. Wolfbeis, "Photonic Crystals for Chemical Sensing and Biosensing," *Angew. Chem. Int. Ed.* **53**(13), 3318–3335 (2014).
18. B. Li, L. Jiang, S. Wang, L. Zhou, H. Xiao, and H.-L. Tsai, "Ultra-Abrupt Tapered Fiber Mach-Zehnder Interferometer Sensors," *Sensors* **11**(6), 5729–5739 (2011).
19. N. N. Klimov, S. Mittal, M. Berger, and Z. Ahmed, "On-chip silicon waveguide Bragg grating photonic temperature sensor," *Opt. Lett.* **40**(17), 3934–3936 (2015).
20. J. N. Anker, W. P. Hall, O. Lyandres, N. C. Shah, J. Zhao, and R. P. Van Duyne, "Biosensing with plasmonic nanosensors," *Nat. Mater.* **7**(6), 442–453 (2008).
21. A. Fernandez Gavela, D. Grajales Garcia, J. C. Ramirez, and L. M. Lechuga, "Last Advances in Silicon-Based Optical Biosensors," *Sensors* **16**(3), 285 (2016).
22. J. T. Robinson, L. Chen, and M. Lipson, "On-chip gas detection in silicon optical microcavities," *Opt. Express* **16**(6), 4296–4301 (2008).
23. H. Xu, M. Hafezi, J. Fan, J. M. Taylor, G. F. Strouse, and Z. Ahmed, "Ultra-sensitive chip-based photonic temperature sensor using ring resonator structures," *Opt. Express* **22**(3), 3098–3104 (2014).
24. B. Bhola, P. Nosovitskiy, H. Mahalingam, and W. H. Steier, "Sol-Gel-Based Integrated Optical Microring Resonator Humidity Sensor," *IEEE Sens. J.* **9**(7), 740–747 (2009).
25. X. Zhao, J. M. Tsai, H. Cai, X. M. Ji, J. Zhou, M. H. Bao, Y. P. Huang, D. L. Kwong, and A. Q. Liu, "A nano-opto-mechanical pressure sensor via ring resonator," *Opt. Express* **20**(8), 8535–8542 (2012).
26. T. Claes, W. Bogaerts, and P. Bienstman, "Experimental characterization of a silicon photonic biosensor consisting of two cascaded ring resonators based on the Vernier-effect and introduction of a curve fitting method for an improved detection limit," *Opt. Express* **18**(22), 22747–22761 (2010).
27. S. M. Grist, S. A. Schmidt, J. Flueckiger, V. Donzella, W. Shi, S. Talebi Fard, J. T. Kirk, D. M. Ratner, K. C. Cheung, and L. Chrostowski, "Silicon photonic micro-disk resonators for label-free biosensing," *Opt. Express* **21**(7), 7994–8006 (2013).
28. K. D. Vos, I. Bartolozzi, E. Schacht, P. Bienstman, and R. Baets, "Silicon-on-Insulator microring resonator for sensitive and label-free biosensing," *Opt. Express* **15**(12), 7610–7615 (2007).
29. V. R. Almeida, Q. Xu, C. A. Barrios, and M. Lipson, "Guiding and confining light in void nanostructure," *Opt. Lett.* **29**(11), 1209–1211 (2004).
30. V. Mere, H. Muthuganesan, Y. Kar, C. V. Kruijdsdijk, and S. K. Selvaraja, "On-Chip Chemical Sensing Using Slot-Waveguide-Based Ring Resonator," *IEEE Sens. J.* **20**(11), 5970–5975 (2020).
31. Y. Hong, H. Ge, and J. Hong, "Compact biosensors based on thin film silicon nitride microring resonators," *J. Phys.: Conf. Ser.* **2012**(1), 012037 (2021).
32. K. B. Gylfason, C. F. Carlborg, A. Kaźmierczak, F. Dortu, H. Sohlström, L. Vivien, C. A. Barrios, W. V. D. Wijngaart, and G. Stemme, "On-chip temperature compensation in an integrated slot-waveguide ring resonator refractive index sensor array," *Opt. Express* **18**(4), 3226–3237 (2010).
33. N. Ashok, Y. L. Lee, and W. Shin, "GeAsSe chalcogenide slot optical waveguide ring resonator for refractive index sensing," in *2017 25th Optical Fiber Sensors Conference (OFS)*, 2017, 1–4.
34. F. Dell'Olio and V. M. N. Passaro, "Optical sensing by optimized silicon slot waveguides," *Opt. Express* **15**(8), 4977–4993 (2007).
35. K. R. Hiremath, "Analytical modal analysis of bent slot waveguides," *J. Opt. Soc. Am. A* **26**(11), 2321–2326 (2009).
36. A. Kargar and C. Y. Chao, "Design and optimization of waveguide sensitivity in slot microring sensors," *J. Opt. Soc. Am. A* **28**(4), 596–603 (2011).
37. W. Zhang, S. Serna, X. Le Roux, L. Vivien, and E. Cassan, "Highly sensitive refractive index sensing by fast detuning the critical coupling condition of slot waveguide ring resonators," *Opt. Lett.* **41**(3), 532–535 (2016).
38. R. Zhang, Z. Yang, M. Zhao, P. Xu, W. Zhang, Z. Kang, J. Zheng, S. Dai, R. Wang, and A. Majumdar, "High quality, high index-contrast chalcogenide microdisk resonators," *Opt. Express* **29**(12), 17775–17783 (2021).
39. Z. Yang, R. Zhang, Z. Wang, P. Xu, W. Zhang, Z. Kang, J. Zheng, S. Dai, R. Wang, and A. Majumdar, "High-Q, submicron-confined chalcogenide microring resonators," *Opt. Express* **29**(21), 33225–33233 (2021).

40. J. Zhou, Q. Du, P. Xu, Y. Zhao, R. Lin, Y. Wu, P. Zhang, W. Zhang, and X. Shen, "Large Nonlinearity and Low Loss Ge-Sb-Se Glass Photonic Devices in Near-Infrared," *IEEE J. Sel. Top. Quantum Electron.* **24**(4), 1–6 (2018).
41. T. Alasaarela, D. Korn, L. Alloatti, A. Säynätjoki, A. Tervonen, R. Palmer, J. Leuthold, W. Freude, and S. Honkanen, "Reduced propagation loss in silicon strip and slot waveguides coated by atomic layer deposition," *Opt. Express* **19**(12), 11529–11538 (2011).
42. A. Säynätjoki, L. Karvonen, T. Alasaarela, X. Tu, T. Liow, M. Hiltunen, A. Tervonen, G. Lo, and S. Honkanen, "Low-loss silicon slot waveguides and couplers fabricated with optical lithography and atomic layer deposition," *Opt. Express* **19**(27), 26275–26282 (2011).
43. W. Zhang, S. Serna, X. L. Roux, C. Alonso-Ramos, L. Vivien, and E. Cassan, "Analysis of silicon-on-insulator slot waveguide ring resonators targeting high Q-factors," *Opt. Lett.* **40**(23), 5566–5569 (2015).
44. D. R. Lide, *CRC handbook of chemistry and physics* (CRC press, 2004), Vol. 85.
45. W. Huang, Y. Luo, W. Zhang, C. Li, L. Li, Z. Yang, and P. Xu, "High-sensitivity refractive index sensor based on Ge-Sb-Se chalcogenide microring resonator," *Infrared Phys. Technol.* **116**, 103792 (2021).
46. T. Yoshie, L. Tang, and S. Y. Su, "Optical microcavity: sensing down to single molecules and atoms," *Sensors* **11**(2), 1972–1991 (2011).
47. T. Claes, J. G. Molera, K. De Vos, E. Schacht, R. Baets, and P. Bienstman, "Label-Free Biosensing With a Slot-Waveguide-Based Ring Resonator in Silicon on Insulator," *IEEE Photonics J.* **1**(3), 197–204 (2009).
48. C. A. Barrios, K. B. Gylfason, B. Sanchez, A. Griol, H. Sohlstrom, M. Holgado, and R. Casquel, "Slot-waveguide biochemical sensor," *Opt. Lett.* **32**(21), 3080–3082 (2007).